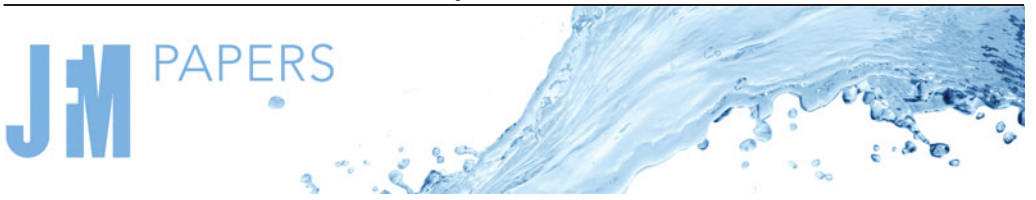
J. Fluid Mech. (2021), *vol*. 920, A13, doi:10.1017/jfm.2021.438



On shock-induced heavy-fluid-layer evolution

Yu Liang[1,2],† **and Xisheng Luo**[2],†

[1]NYUAD Research Institute, New York University Abu Dhabi, Abu Dhabi 129188, UAE

[2]Advanced Propulsion Laboratory, Department of Modern Mechanics, University of Science and Technology of China, Hefei 230026, PR China

(Received 5 February 2021; revised 29 March 2021; accepted 10 May 2021)

Investigation on the shock-induced finite-thickness fluid-layer evolution is very desirable but remains a challenge because it not only involves both the Richtmyer–Meshkov instability (RMI) and the Rayleigh–Taylor instability (RTI), but also strongly depends on the waves reverberated inside the layer. We experimentally and theoretically examined the evolution of a shocked SF_6 gas layer with a finite thickness surrounded by air. Specifically, three kinds of quasi-one-dimensional SF_6 gas layers with different layer thicknesses are generated to study the wave patterns and interface motions, and six types of quasi-two-dimensional SF_6 gas layers with diverse layer thicknesses and amplitude combinations are created to explore the interfacial instabilities of the layer. When the initial fluid layer is thin, the two interfaces of the layer coalesce at a late time. The present study is the first to report that except for the RMI induced by a shock wave on the two interfaces, the rarefaction waves (RW) inside the fluid layer induce the additional RTI and decompression effect on the first interface, and the compression waves (CW) inside the fluid layer cause the additional Rayleigh–Taylor stabilisation (RTS) and compression effect on the second interface. A general one-dimensional theory is established to describe the motions of the two interfaces. Linear and nonlinear models are successfully established by considering the interface-coupling effect on the RMI and the additional interfacial instabilities induced by these waves inside the heavy fluid layer. The established models predict well the perturbation growths on the two interfaces at all regimes.

Key words: shock waves

1. Introduction

Rayleigh–Taylor instability (RTI) develops when light fluids accelerate heavy fluids (Rayleigh 1883; Taylor 1950), then bubbles (the light fluid penetrating the heavy one) and spikes (the heavy fluid penetrating the light one) arise, and turbulence is

† Email addresses for correspondence: yu.liang@nyu.edu, xluo@ustc.edu.cn

© The Author(s), 2021. Published by Cambridge University Press

https://doi.org/10.1017/jfm.2021.438 Published online by Cambridge University Press

finally induced. A similar phenomenon is observed in Richtmyer–Meshkov instability (RMI), which occurs when an interface separating two kinds of fluids is impulsively accelerated by a shock wave (Richtmyer 1960; Meshkov 1969). Both instabilities play essential roles in various industrial and scientific fields, such as inertial confinement fusion (ICF) (Lindl *et al.* 2014) and supernova explosion (Kuranz *et al.* 2018). For example, RMI occurs when the shocks generated by intense lasers or X-rays interact with the ablator layer or the fuel layer of an ICF capsule. RMI determines the seed of RTI during the implosion in ICF. Finally, the mixing induced by RMI and RTI significantly reduces and even eliminates the thermonuclear yield. In addition, the shocks generated by star collapse in a supernova interact with the multi-layer heavy elements throughout interstellar space. The mixing induced by RMI and RTI shapes the filament structures in the remnant of the historical supernova of 1054 AD. Therefore, it is significant to investigate the RMI and RTI involved in the interaction of a shock wave and a finite-thickness fluid layer. However, most previous work has focused on the evolution of a single-mode interface with a semi-infinite thickness induced by these two instabilities (Sharp 1984; Brouillette 2002; Zhou 2017*a*, *b*; Zhai *et al.* 2018; Banerjee 2020).

Theoretically, Taylor (1950) was the first to consider the RTI of a finite-thickness liquid layer and found that the interface-coupling effect is significant when the fluid-layer thickness is sufficiently small. Subsequently, Ott (1972) proposed a nonlinear solution describing the RTI of a thin massless fluid layer and explained the formation of bubbles and spikes. Mikaelian (1982, 1985, 1990, 1995, 1996) deduced linear solutions for quantifying the perturbation growths induced by RTI and RMI on an arbitrary number of stratified fluids. If the number of stratified fluids is larger than three, it is difficult to infer the analytical solutions. Jacobs *et al.* (1995) considered the RMI of a heavy fluid layer and deduced a linear model for the perturbation growth rates at two sides of the fluid layer and a vortex model for the mixing width growth of the fluid layer. Wang *et al.* (2014) analysed the RTI of a fluid layer in a vacuum and proposed a third-order weakly nonlinear solution for the perturbation growths on two sides of the fluid layer. Subsequently, Liu *et al.* (2018*b*) discussed the RMI of two superimposed fluid layers in a vacuum and inferred a third-order weakly nonlinear solution for the middle-interface perturbation growth.

Experimentally, Jacobs *et al.* (1993) adopted the gas curtain technique to investigate the shock-induced evolution of a thin SF_6 gas layer and observed three specific flow patterns. Budzinski, Benjamin & Jacobs (1994) concluded that the three distinct flow patterns are ascribed to different perturbation amplitudes at two sides of the fluid layer. Jacobs *et al.* (1995) found it difficult to predict or control the flow pattern because the initial shape of the gas curtain is not controllable. Prestridge *et al.* (2000) measured the circulation on a shocked gas curtain and validated the vortex model proposed by Jacobs *et al.* (1995). Recently, shock-induced inclined SF_6 curtain evolution was explored (Olmstead *et al.* 2017; Romero *et al.* 2021), and it was found that the pressure waves inside the heavy gas are responsible for the scale selection in fully three-dimensional initial conditions, resulting in the Kelvin–Helmholtz instability (KHI) becoming dominant. The soap-film technique was recently utilised to study the interaction of a converging shock wave and a heavy or light fluid layer (Ding *et al.* 2019; Li *et al.* 2020; Sun *et al.* 2020). Compared with the planar RMI, the additional geometric convergent effect (Bell 1951; Plesset 1954) and Rayleigh–Taylor stabilisation (RTS) effect induced by high pressures near the focusing point (Luo *et al.* 2018), introduced by the cylindrical or spherical RMI, complicate the analysis on the fluid-layer evolution. Our previous work (Liang *et al.* 2020*a*) extended the soap-film technique and investigated the RMI of five kinds of SF_6 gas layers in the planar geometry. Except for examining the conclusion of Budzinski *et al.* (1994) that amplitudes

https://doi.org/10.1017/jfm.2021.438 Published online by Cambridge University Press

of the two interfaces determine the flow patterns, Liang *et al.* (2020*a*) discovered that the rarefaction waves (RW) reflected from the second interface induce the additional RTI of the first interface, which coincides with previous numerical studies (de Frahan, Movahed & Johnsen 2015).

Although significant progress in the study of shock-induced fluid-layer evolution has been made, the influence of the fluid-layer thickness on the layer evolution has not been experimentally studied because the realisation of such experiments is difficult. For example, the fluid-layer thickness is normally fixed by the gas-curtain generation device. However, the fluid-layer thickness could be used advantageously to minimise the amount of mixing and spike penetration in ICF capsules (Drake 2018), and an appropriate thickness of the fluid layer even results in the freeze-out of the first interface perturbation growth (Mikaelian 1996). Therefore, it is very desirable to investigate the influence of the fluid-layer thickness on the layer evolution, especially when the fluid layer is thin and the interface-coupling effect is prominent. Previous studies (de Frahan *et al.* 2015; Liang *et al.* 2020*a*) only considered the RW but ignored the compression waves (CW) inside a heavy fluid layer. As a result, previous studies only recognised the instability induced by the RW but neglected the CW stabilisation effect involved in the shock-induced heavy-fluid-layer evolution. In this work, to establish a general one-dimensional (1-D) theory for describing the wave patterns and interface motions, we first experimentally investigate the interaction of a shock wave and three kinds of quasi-1-D SF_6 gas layers by varying the fluid-layer thickness. Then, to explore the interfacial instabilities at both sides of a fluid layer, we experimentally study the interaction of a shock wave with six kinds of quasi-two-dimensional (2-D) SF_6 gas layers with different fluid-layer thicknesses and amplitude combinations. Linear and nonlinear theories will be established to describe the perturbation growths induced by various interfacial instabilities at both sides of the heavy fluid layer. We will explore the shock-induced light-fluid-layer evolution in a future study.

2. Experimental method

To create an SF_6 gas layer, the extended soap-film technique is utilised to generate two shape-controllable and discontinuous interfaces, mainly eliminating the additional short-wavelength perturbations, diffusion layer and three-dimensionality (Liu *et al.* 2018*a*; Liang *et al.* 2019). As shown in figure 1(*a*), three transparent devices with a width of 140 mm and a height of 10 mm are first manufactured using transparent acrylic sheets with a thickness of 3 mm. The adjacent boundaries of the middle device are carefully engraved to be of a sinusoidal shape with a depth of 1.8 mm. Four thin filaments with a height of 2.0 mm are attached to the inner surfaces of the upper and lower plates at two sides of the middle device in order to restrict the soap film. In this way the filament bulges in the flow field with only 0.2 mm height and its influence on the flow is limited (Liang *et al.* 2020*a*). Before the interface formation, the filaments are properly wetted by a soap solution with a mass fraction of 78 % distilled water, 2 % sodium oleate and 20 % glycerine. First, a small rectangular frame with moderate soap solutions dipped on its borders is pulled along the sinusoidal filaments on both sides of the middle device, and two soap-film interfaces are generated and the closed space is formed. Second, SF_6 is pumped into the closed space through an inflow hole to discharge air inside through an outflow hole. An oxygen concentration detector is placed at the outflow hole to ensure the SF_6 purity inside the closed space. Subsequently, the inflow and outflow holes are sealed. Finally, the left and right transparent devices are gently connected to the middle device, and the combined one is inserted into the test section of a shock-tube.

https://doi.org/10.1017/jfm.2021.438 Published online by Cambridge University Press

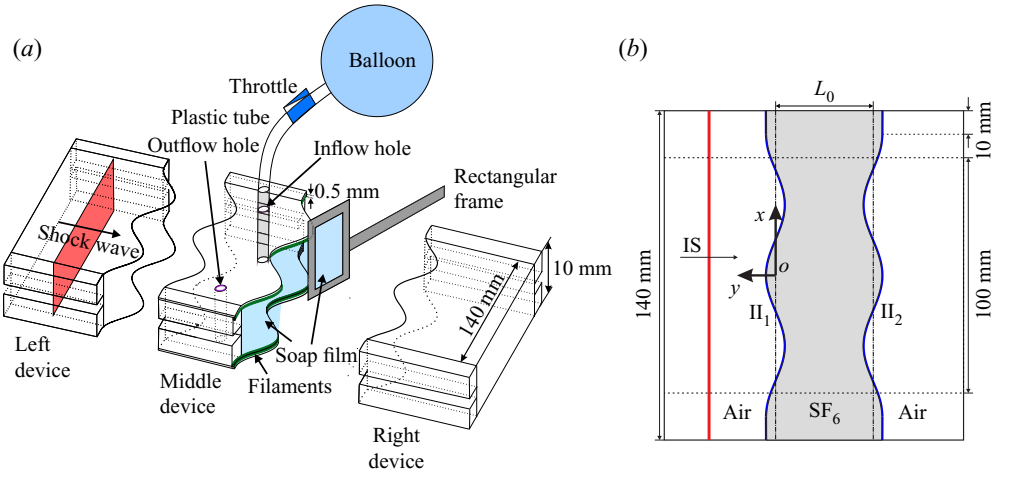


Figure 1. Schematics of (*a*) the soap-film interface generation and (*b*) the initial configuration studied in the present work. Here L_0 denotes the fluid-layer thickness, II_1 denotes the initial first interface, II_2 denotes the initial second interface and IS denotes the incident shock wave.

Case	L10-1D	L30-1D	L50-1D	L10-IP	L10-AP	L30-IP	L30-AP	L50-IP	L50-AP
a_1^0 (mm)	0	0	0	2	2	2	2	2	2
a_2^0 (mm)	0	0	0	2	−2	2	−2	2	−2
L_0 (mm)	10	30	50	10	10	30	30	50	50

Table 1. Initial physical parameters of an SF_6 fluid layer for different cases. Here, a_1^0 (a_2^0) represents the initial amplitude of the first (second) interface.

In the Cartesian coordinate system, as sketched in figure 1(*b*), the perturbations on the two interfaces are single mode as $y = a_n^0 \cos(kx)$ within the range of $x \in [-60, 60]$ mm, where a_n^0 denotes the initial amplitude of the nth interface with $n = 1$ and 2 and k the wavenumber of the two interfaces. In this work, $k = 104.7$ m^{-1}, while a_1^0 and a_2^0 in all cases are listed in table 1. The initial thickness of a fluid layer (L_0) is defined as the distance between the average positions of the initial first interface (II_1) with the initial second interface (II_2). In all, we investigate three kinds of quasi-1-D SF_6 gas layers with no perturbations and six kinds of quasi-2-D SF_6 gas layers with three fluid-layer thicknesses and two amplitude combinations. Here, we define the three cases (i.e. cases L10-IP, L30-IP and L50-IP) with $a_2^0 > 0$ as in-phase cases and the three cases (i.e. cases L10-AP, L30-AP and L50-AP) with $a_2^0 < 0$ as anti-phase cases. To minimise the wall effect of the shock tube on the interface evolution, a short flat part with 10 mm on each side of the two interfaces is adopted. Its influence on the interface evolution is limited (Luo *et al.* 2019). The surrounding gas outside the fluid layer is air. The test gas inside the fluid layer is a mixture of SF_6 and air, and the mass fraction of SF_6 is 0.97 ± 0.01. The incident shock wave (IS) travels from left to right.

The ambient pressure and temperature are 101.3 kPa and 295.5 ± 1.0 K, respectively. The Mach number of the IS is 1.20 ± 0.01, the velocity of the IS (u_s) is 412 ± 2 m s^{-1}, the speed of the transmitted shock (TS_1) after the IS passes the II_1, i.e. u_{t1}, is $188 \pm$

https://doi.org/10.1017/jfm.2021.438 Published online by Cambridge University Press

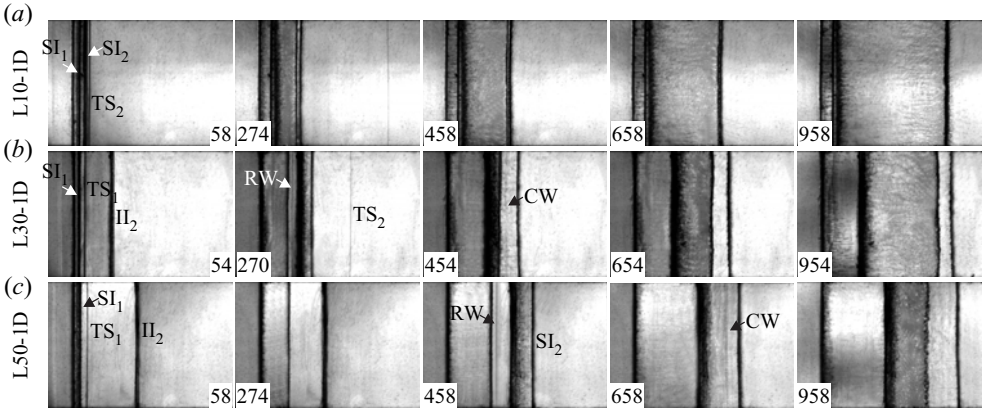


Figure 2. Schlieren images of the shock-induced quasi-1-D SF_6 gas-layer evolution in cases (*a*) L10-1D, (*b*) L30-1D and (*c*) L50-1D. Here SI_1 (SI_2) denotes the shocked first (second) interface, TS_1 denotes the transmitted shock after the IS impacts the II_1 and TS_2 denotes the transmitted shock after the TS_1 impacts the II_2. Numbers denote time in microseconds.

2 m s^{-1}, the speed of the transmitted shock (TS_2) after the TS_1 passes the II_2, i.e. u_{t2}, is 406 ± 2 m s^{-1}. Based on the 1-D gas dynamics theory (Han & Yin 1993), the jump speed of the first interface (Δu_1) is 72 ± 1 m s^{-1}, and the jump speed of the second interface (Δu_2) is 94 ± 1 m s^{-1}. Here, we define the Atwood number of gas layer (A) as $(\rho_2 - \rho_1)/(\rho_2 + \rho_1)$ with ρ_1 and ρ_2 the density of air outside the fluid layer and the test gas inside the fluid layer, respectively. A equals 0.63 ± 0.01 in this work. The flow field is monitored by high-speed schlieren photography. The high-speed video camera (FASTCAM SA5, Photron Limited) is 60 000 f.p.s. with a shutter time of 1 μs. The spatial resolution of schlieren images is 0.4 mm $pixel^{-1}$. The flow-field visualisation is limited within the range of $x \in [-50, 50]$ mm, as shown in figure 1(*b*).

3. Results and discussion

3.1. *Quasi-1-D experimental results and analysis*

Schlieren images of the shock-induced quasi-1-D SF_6 gas layer evolution are shown in figures 2(*a*)–2(*c*) for $L_0 = 10$, 30 and 50 mm, respectively. The moment when the IS impacts the average position of II_1 is defined as $t = 0$. Taking the L50-1D case as an example, the wave patterns and interface motions are discussed in detail. After the IS impacts the II_1, the TS_1 is generated, and the shocked first interface (SI_1) begins to move forwards (58 μs). Then the TS_1 impacts the II_2 (274 μs), and the TS_2 moves outside the fluid layer followed by the shocked second interface (SI_2). Meanwhile, the RW is reflected inside the fluid layer and moves towards the SI_1 (458 μs), because the second interface is a slow/fast interface relative to the RW motion. Subsequently, the RW impacts and accelerates the SI_1. Meanwhile, the CW is reflected inside the fluid layer (658 μs) and moves towards the SI_2 because the first interface is a slow/fast interface relative to the CW motion. Later, the CW impacts and accelerates the SI_2. After the CW passes the SI_2, the waves reflected inside the fluid layer are feeble and therefore ignored in this work. Finally, all waves refract outside the fluid layer and the interfaces at two sides of the fluid layer move with the same speed (958 μs). Notably, owing to the limited L_0 in the L10-1D case, the two interfaces coalesce to one at a late time (958 μs).

https://doi.org/10.1017/jfm.2021.438 Published online by Cambridge University Press

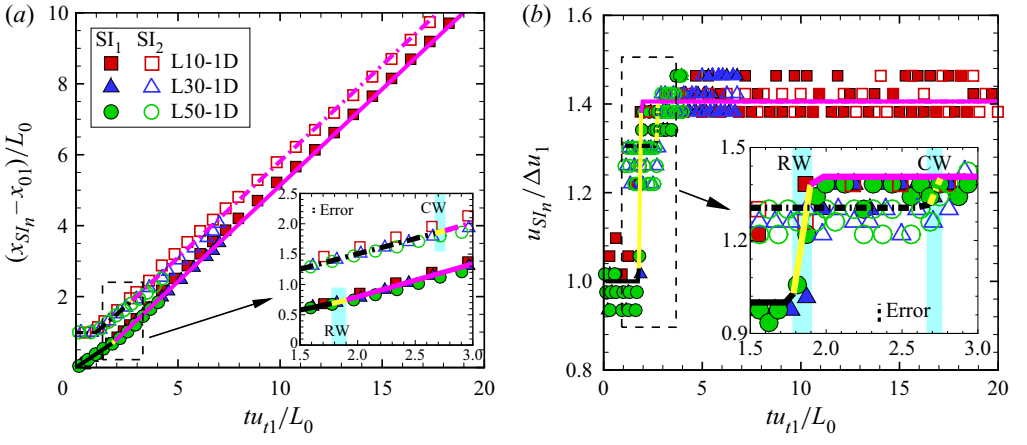


Figure 3. The dimensionless displacements (*a*) and velocities (*b*) of the first interface (solid symbols) and the second interfaces (hollow symbols). Black, yellow and purple solid (dash-dotted) lines represent the 1-D theory predictions for the first (second) interface in stages I, II and III, respectively. The light blue zones in the insets indicate the interaction of the RW (CW) with the SI_1 (SI_2). The black dashed lines in the insets represent the scale of measurement error.

The interface displacements (x_{SI_n}) and velocities (u_{SI_n}) of the two interfaces are measured from experiments ($n = 1$ for the first interface and $n = 2$ for the second interface), as shown in figures 3(*a*) and 3(*b*), respectively. We measure the positions of the top, middle and bottom points of both interfaces from each schlieren image and calculate the average value of the three-point positions as the interface position. The pixel size of schlieren images introduces the experimental measurement uncertainty, which is 0.4 mm in this work. The size of error bars equals the size of symbols representing the experimental results. Time is scaled as tu_{t1}/L_0, interface displacement is scaled as $(x_{SI_n} - x_{01})/L_0$ with x_{01} the initial position of the first interface and interface velocity is scaled as $u_{SI_n}/\Delta u_1$, respectively. The dimensionless displacements and velocities of the first (second) interface converge in all L_0 cases, especially the interface velocity increment of the first (second) interface during the interaction of the RW (CW) with the first (second) interface, which indicates that we can establish a general 1-D theory applicable to an arbitrary fluid-layer thickness to describe the behaviour of the two interfaces.

First, we define the specific times when the RW and CW are initially generated as t_r^0 and t_c^0, the time when the RW impacts the SI_1 as t_r^* and the time when the CW impacts the SI_2 as t_c^*, as sketched in figure 4, respectively. Then t_r^0, t_c^0, t_r^* and t_c^* can be calculated as

$$\left.\begin{aligned} t_r^0 &= \frac{L_0}{u_{t1}}, \\ t_c^0 = t_r^* &= t_r^0 + \frac{L_0(1-\Delta u_1/u_{t1})}{c_1}, \\ t_c^* &= t_r^* + \frac{L_0}{c_1^*}\left[1 - \frac{\Delta u_1}{u_{t1}} - \frac{(1-\Delta v_1/v_{t1})(\Delta u_2 - \Delta u_1)}{c_1}\right], \end{aligned}\right\} \tag{3.1}$$

where c_1 and c_1^* are the sound speeds of the test gas between the SI_1 with TS_1, and between the SI_2 with the RW tail, respectively. Based on 1-D gas dynamics theory

https://doi.org/10.1017/jfm.2021.438 Published online by Cambridge University Press

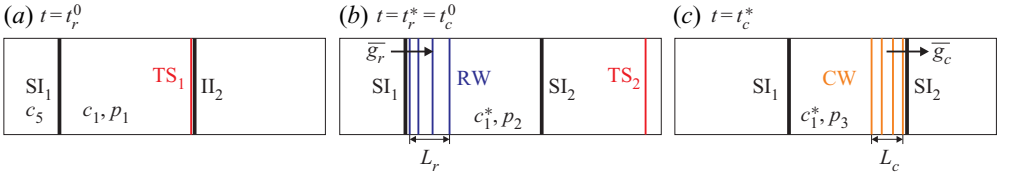


Figure 4. Sketches of (*a*) the interaction of TS_1 and II_2, (*b*) the interaction of the RW and SI_1 and (*c*) the interaction of the CW and SI_2. Here,c_1 represents the sound speed of the test gas between the SI_1 with TS_1, c_1^* denotes the sound speed of the test gas between the SI_2 with RW tail, c_5 denotes the sound speed of air after the IS impacts II_1, p_1 denotes the pressure of the flow behind the TS_1, p_2 denotes the pressure of the flow behind the RW and p_3 denotes the pressure of the flow behind the CW tail.

Case	L10-1D	L30-1D	L50-1D	L10-IP	L10-AP	L30-IP	L30-AP	L50-IP	L50-AP
t_r^0	53	180	267	54	54	162	158	271	267
t_c^0	95	284	474	96	96	288	281	480	474
t_r^*	95	284	474	96	96	288	281	480	474
t_c^*	143	428	713	145	145	434	423	725	713
L_r	1.0	2.9	4.8	1.0	1.0	3.0	2.8	4.9	4.8
L_c	0.7	2.0	3.4	0.7	0.7	2.1	2.2	3.5	3.4
δt_r	6.9	20.6	34.4	7.2	7.2	21.4	21.3	35.9	34.4
δt_c	4.5	13.5	22.5	4.7	4.7	14.4	14.3	23.5	22.5
$\overline{g_r}$	4.3	1.4	8.5	4.2	4.2	1.4	1.3	8.3	8.5
$\overline{g_c}$	1.6	5.4	3.2	1.6	1.6	5.1	5.2	3.1	3.2
t_r^+	50	267	474	713	4.8	3.4	34.4	22.5	8.5
t_c^+	10	54	96	145	1.0	0.7	7.2	4.7	4.2

Table 2. Physical parameters of an SF_6 fluid layer calculated by the 1-D theory established in this work (3.4) and (3.5). Here t_r^0 (t_c^0) denotes the time when RW (CW) is initially generated, t_r^* (t_c^*) denotes the time when the RW (CW) impacts the first (second) interface, L_r (L_c) denotes the streamwise length of the RW (CW) at t_r^* (t_c^*), δt_r (δt_c) denotes the interaction time of the RW (CW) with the first (second) interface, $\overline{g_r}$ ($\overline{g_c}$) denotes the average acceleration imposed on the first (second) interface by the RW (CW) and t_r^+ (t_c^+) denotes the time when the RW (CW) tail leaves the first (second) interface. The units for time, length and acceleration are microseconds, millimetres and 10^6 m s^{-2}, respectively.

(Han & Yin 1993), c_1 and c_1^* are 148 ± 1 m s^{-1} and 146 ± 1 m s^{-1}, respectively. Then t_r^0, t_c^0, t_r^* and t_c^* are derived in all cases, as listed in table 2. As L_0 increases, t_r^0, t_c^0, t_r^* and t_c^* increase. However, the dimensionless times, i.e. $t_r^0 v_{t1}/L_0$, $t_c^0 v_{t1}/L_0$, $t_r^* v_{t1}/L_0$ and $t_c^* v_{t1}/L_0$, equal 1.00, 1.78, 1.78 and 2.68 in all cases, which indicates that the motions of waves inside the fluid layer are not influenced by the fluid-layer thickness.

Second, as sketched in figure 4, we define the streamwise length of the RW when its head impacts SI_1 as L_r, the streamwise length of the CW when its head impacts SI_2 as L_c, the interaction time of the RW with SI_1 as δt_r, the interaction time of the CW with SI_2 as δt_c, the average acceleration that the RW imposes on the SI_1 as $\overline{g_r}$ and the average acceleration that the CW imposes on the SI_2 as $\overline{g_c}$, respectively. Notably, although the acceleration imposed by the RW on the SI_1 during δt_r, and the acceleration imposed by the CW on the SI_2 during δt_c are not constant (Morgan *et al.* 2018; Liang *et al.* 2020*b*), to simplify the analysis, the accelerations are taken as constant (Morgan, Likhachev & Jacobs 2016; Liang *et al.* 2020*a*), which can be regarded as a first-order approximation. To calculate the L_r, L_c, δt_r, δt_c, $\overline{g_r}$ and $\overline{g_c}$, the final velocity (u_{fn}) of the fluid layer, i.e. the

https://doi.org/10.1017/jfm.2021.438 Published online by Cambridge University Press

speed of the SI_1 after the RW accelerates it, should be derived at first. Based on 1-D gas dynamics theory (Velikovich & Phillips 1996; Liang *et al.* 2020*b*),

$$u_{fn} = \Delta u_1 - \frac{2c_1}{\gamma_1 - 1}\left[p_{21}^{(\gamma_1-1)/2\gamma_1} - 1\right] + \frac{\sqrt{2}c_1(p_{31}/p_{21} - 1)}{\sqrt{\gamma_1(\gamma_1+1)p_{31}/p_{21}}}, \tag{3.2}$$

where γ_1 is the specific heat ratio of the test gas inside the fluid layer and equals 1.1, p_{21} is the ratio of the pressure of the flow behind the TS_2 (p_2) to the pressure of the flow behind the TS_1 (p_1), as sketched in figure 4 and which equals 0.85. The only unknown parameter p_{31}, i.e. the ratio of the pressure of the flow behind the CW tail (p_3) to p_1, satisfies

$$\frac{c_5}{c_1} = \frac{\gamma_5 - 1}{p_{31}^{(\gamma_5-1)/2\gamma_5} - 1}\left\{\frac{2}{\gamma_1 - 1}\left[p_{21}^{(\gamma_1-1)/2\gamma_1} - 1\right] - \frac{\sqrt{2}(p_{31}/p_{21} - 1)p_{21}^{(\gamma_1-1)/2\gamma_1}}{\sqrt{(\gamma_1+1)\gamma_1 p_{31}/p_{21} + (\gamma_1-1)\gamma_1}}\right\}, \tag{3.3}$$

where c_5 is the sound speed of air after the IS impacts II_1 and equals 369 ± 2 m s^{-1} and γ_5 is the specific heat ratio of air and equals 1.4. Then the p_{31} and u_{fn} can be calculated as 0.90 and 101 ± 1 m s^{-1} by solving (3.2) and (3.3). Subsequently, we can deduce the expressions for L_r, δt_r and $\overline{g_r}$ as

$$\left.\begin{aligned} L_r &= \frac{L_0(1 - \Delta u_1/u_{t1})(\gamma_1+1)(\Delta u_2 - \Delta u_1)}{2c_1}, \\ \delta t_r &= \frac{2L_r}{\gamma_1(\Delta u_1 - \Delta u_2) + u_{fn} - \Delta u_1 + 2c_1}, \\ \overline{g_r} &= \frac{u_{fn} - \Delta u_1}{\delta t_r}. \end{aligned}\right\} \tag{3.4}$$

In this work, because the waves reflected inside the fluid layer after the CW impacts the SI_2 are ignored, the sound speed of the test gas between the SI_1 with the CW tail equals c_1^*, as sketched in figure 4(*c*). Then the expressions for L_c, δt_c and $\overline{g_c}$ are

$$\left.\begin{aligned} L_c &= \delta t_r\left[u_{fn} + c_1^* + \frac{1}{2}(\Delta u_1 - \Delta u_2)\right] - (t_c^* - t_r^*)(u_{fn} - \Delta u_2) - \frac{1}{2}\overline{g_r}(\delta t_r)^2, \\ \delta t_c &= \frac{2L_c}{(u_{fn} - \Delta u_2) + 2c_1^*}, \\ \overline{g_c} &= \frac{u_{fn} - \Delta u_2}{\delta t_c}. \end{aligned}\right\} \tag{3.5}$$

The values of L_r, L_c, δt_r, δt_c, $\overline{g_r}$ and $\overline{g_c}$ are listed in table 2. As L_0 increases, L_r, L_c, δt_r and δt_c increase, but $\overline{g_r}$ and $\overline{g_c}$ decrease, which indicates the strengths of the RW and CW become weaker.

In summary, we establish a general 1-D theory to describe the motions of the first interface and second interface in three stages. For the first interface: (I) uniform motion with Δu_1 during $t_r^* > t > 0$; (II) acceleration with $\overline{g_r}$ during $t_r^+ > t > t_r^*$ with $t_r^+ = t_r^* + \delta t_r$ and (III) uniform motion with u_{fn} during $t > t_r^+$. For the second interface: (I) uniform motion with the Δu_2 during $t_c^* > t > t_r^0$, (II) acceleration with $\overline{g_c}$ during $t_c^+ > t > t_c^*$ with $t_c^+ = t_c^* + \delta t_c$, and (III) uniform motion with u_{fn} during $t > t_c^* + \delta t_c$. The values of t_r^+ and

https://doi.org/10.1017/jfm.2021.438 Published online by Cambridge University Press

t_c^+ are listed in table 2. The predictions of the 1-D theory for the interface motions in stages I, II and III are marked with black, yellow and purple lines, respectively, as represented with solid lines for the first interface and dash-dotted lines for the second interface in figures 3(*a*) and 3(*b*), which agree well with the experimental results.

3.2. *Quasi-2-D experimental results and analysis*

Schlieren images of six kinds of the shock-induced quasi-2-D SF_6 fluid-layer evolution are shown in figures 5(*a*)–5(*f*). Except for the actual timescale, we also provide a dimensionless timescale, i.e. τ_R ($=kv_1^R t$, in which v_1^R is the Richtmyer growth rate calculated with (3.6)). Taking the L30-IP case as an example, the deformations of the two interfaces are discussed in detail. After the IS impacts the perturbed II_1, the perturbation on the SI_1 grows, and a rippled TS_1 moves towards II_2 (58 μs, $\tau_R = 0.05$). After the TS_1 impacts the perturbed II_2, the rippled RW is reflected inside the fluid layer and moves towards SI_1 (258 μs, $\tau_R = 0.21$). Meanwhile, the perturbation on SI_2 decreases gradually owing to the phase reversal process (Brouillette 2002). Subsequently, after the RW impacts SI_1, the rippled CW is reflected inside the fluid layer and moves towards SI_2, and the perturbation on SI_2 nearly disappears at 389 μs, $\tau_R = 0.32$). Later, the perturbation on SI_2 increases with the phase opposite to SI_1 (673 μs, $\tau_R = 0.56$). Finally, vortices appear on the spike of SI_1 (956 μs, $\tau_R = 0.79$), which are ascribed to the KHI. The final phase of the SI_2 in the three in-phase cases is opposite to that of the SI_1, whereas the final phase of the SI_2 in the three anti-phase cases is the same as that of the SI_1. The two interfacial deformations in the L50-IP and L50-AP cases are similar to the corresponding L30-IP and L30-AP cases. Nevertheless, the late-time interface morphologies of the two interfaces in the L10-IP and L10-AP cases are different from the other four large L_0 cases. In the L10-IP case at 959 μs ($\tau_R = 0.79$), bubbles of the two interfaces coalesce while spikes grow oppositely with their sizes much smaller than the other four large L_0 cases. In the L10-AP case at 965 μs ($\tau_R = 0.80$), all structures of the two interfaces coalesce. The whole fluid layer evolves into a 'sinuous' shape, which qualitatively agrees with the shock-induced gas-curtain morphology reported previously (Jacobs *et al.* 1993; Budzinski *et al.* 1994; Jacobs *et al.* 1995).

The amplitudes of the first and second interfaces, a_1 and a_2, are defined as half of the streamwise distance between the spike tip with the bubble tip of the first interface and second interface, respectively. We measure the positions of two bubble tips and one spike tip of the first interface from each schlieren image, and calculate the a_1 by the average of two bubble tip positions minus the spike tip position. We measure the positions of two bubble (spike) tips and one spike (bubble) tip of the second interface in the three in-phase (anti-phase) cases from each schlieren image, and calculate the a_2 by the average of two bubble (spike) tip positions minus the spike (bubble) tip position. The amplitude growths on the two interfaces are divided into three stages based on the 1-D theory established in this work: I. Linear stage ($t_r^* > t > 0$ for the first interface, $t_c^* > t > t_r^0$ for the second interface), II. Early nonlinear stage ($t_r^+ > t > t_r^*$ for the first interface, $t_c^+ > t > t_c^*$ for the second interface) and III. Late nonlinear stage ($t > t_r^+$ for the first interface, $t > t_c^+$ for the secondinterface).

In the linear stage, only RMI decides the amplitude growths of the two interfaces. The linear growth rates of the amplitude of the two interfaces, v_1^{exp} and v_2^{exp}, are acquired by linear fitting the two interface amplitudes measured from experiments, as listed in table 3. For cases with the same L_0, the v_1^{exp} and v_2^{exp} are larger in the three anti-phase cases than

https://doi.org/10.1017/jfm.2021.438 Published online by Cambridge University Press

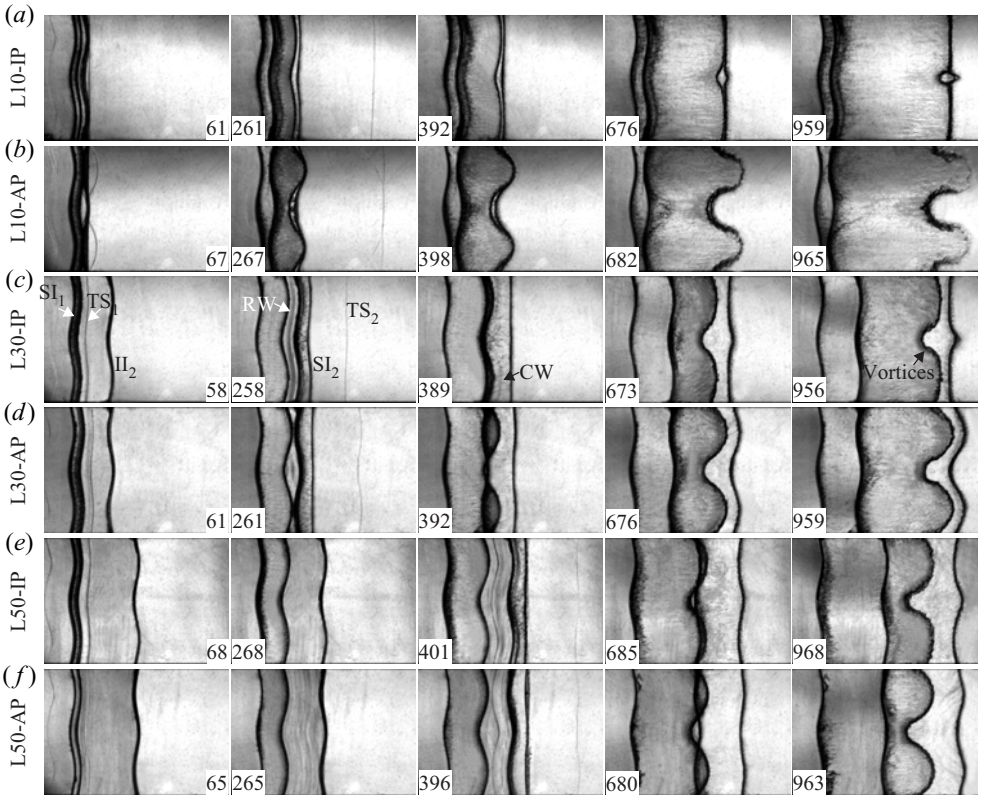


Figure 5. Schlieren images of the shock-induced quasi-2-D SF_6 fluid-layer evolution in cases (*a*) L10-IP, (*b*) L10-AP, (*c*) L30-IP, (*d*) L30-AP, (*e*) L50-IP and (*f*) L50-AP. Numbers denote time in microseconds.

those in the three in-phase cases. For cases with the same amplitude combinations, as the L_0 increases, the v_1^{exp} and v_2^{exp} increase in the three in-phase cases, but decrease in the three anti-phase cases. In order to determine the difference between the classical RMI of a semi-infinite single-mode interface with the RMI of a heavy fluid layer, the Richtmyer impulsive theory (Richtmyer 1960) is adopted to calculate the first interface amplitude growth rate (v_1^R), and the Meyer–Blewett impulsive theory (Meyer & Blewett 1972) is utilised to obtain the second interface amplitude growth rate (v_2^{MB}) as

$$\left.\begin{aligned} v_1^R &= Z_1 a_1^0 k \Delta u_1 A, \\ v_2^{MB} &= -\frac{(Z_2+1) a_2^0 k \Delta u_2 A}{2}, \end{aligned}\right\} \tag{3.6}$$

with two compression factors $Z_1 = 1 - \Delta u_1/v_s$ and $Z_2 = 1 - \Delta u_2/v_{t1}$. The values of v_1^R and v_2^{MB} in all cases are listed in table 3. Here v_1^{exp} is smaller than v_1^R in the three in-phase cases, and v_2^{exp} is larger than v_2^{MB} in the three anti-phase cases. The difference between the experimental result and the corresponding theoretical result is pronounced when L_0 is limited, which agrees with previous findings (Ott 1972). As a result, the coupling between the two interfaces of a fluid layer, i.e. the interface-coupling effect, plays a vital role in influencing RMI development (Jacobs *et al.* 1995; Mikaelian 1996; Liang *et al.* 2020*a*), especially when the initial fluid-layer thickness is small.

https://doi.org/10.1017/jfm.2021.438 Published online by Cambridge University Press

Case	L10-IP	L10-AP	L30-IP	L30-AP	L50-IP	L50-AP
v_1^{exp}	3.1 ± 0.6	14.3 ± 1.0	6.5 ± 0.8	8.8 ± 0.8	7.8 ± 0.8	8.0 ± 0.8
v_2^{exp}	-2.0 ± 0.5	20.0 ± 1.6	-6.7 ± 0.8	10.5 ± 1.0	-8.7 ± 0.8	10.1 ± 1.0
v_1^R	7.9	7.9	7.9	7.8	7.9	7.8
v_2^{MB}	-6.3	6.3	-6.3	6.2	-6.3	6.2
v_1^l	3.5	14.7	6.3	9.6	7.4	8.2
v_2^l	-2.4	22.5	-7.1	11.8	-8.7	9.9
v_{1b}^+	13.6	24.5	16.0	18.6	17.1	17.0
v_{1s}^+	14.7	25.8	17.3	19.9	18.9	18.5
v_{2b}^+	-0.1	20.5	-3.2	9.6	-6.3	7.8
v_{2s}^+	-0.0	20.1	-2.9	9.2	-5.9	7.4

Table 3. The amplitude growth rates of the two interfaces in different cases. Here, v_1^{exp} (v_2^{exp}) denotes the linear amplitude growth rate of the first (second) interface measured from experiments, v_1^R (v_2^{MB}) denotes the linear amplitude growth rate of the first (second) interface calculated with the Richtmyer (Meyer–Blewett) impulsive theory (3.6), v_1^l (v_2^l) denotes the linear amplitude growth rate of the first (second) interface calculated with the mJ model (3.9) and (3.10*a*,*b*) and $v_{1b/1s}^+$ ($v_{2b/2s}^+$) denotes the early nonlinear bubble/spike amplitude growth rate of the first (second) interface at t_r^+ (t_c^+) calculated with the mZG model (3.11) and (3.12). The unit for velocity is m s^{-1}.

Jacobs *et al.* (1995) introduced a linear solution (J model) for describing the amplitude growth rates of the first interface (v_1^l) and second interface (v_2^l) by considering the interface-coupling effect on the RMI,

$$\left.\begin{aligned} v_1^l &= \frac{k\Delta u_1\left[A_t(a_1^0 - a_2^0) + A_c(a_1^0 + a_2^0)\right]}{2}, \\ v_2^l &= \frac{k\Delta u_2\left[A_t(a_1^0 - a_2^0) - A_c(a_1^0 + a_2^0)\right]}{2}, \end{aligned}\right\} \tag{3.7}$$

with two modified Atwood numbers,

$$A_t = \frac{\rho_2 - \rho_1}{\rho_2 \tanh(kL_0/2) + \rho_1} \quad \text{and} \quad A_c = \frac{\rho_2 - \rho_1}{\rho_2 \coth(kL_0/2) + \rho_1}. \tag{3.8a,b}$$

When $L_0 \to \infty$, $A_t = A_c = A$ and the J model reduces to the Richtmyer impulsive theory. Notably, the amplitude growth rate of one interface is influenced by the initial amplitude of the other interface, which indicates the interface-coupling effect. The J model adopts the pre-shock parameters and ignores the shock compression effect. Here, we modify the J model for the first interface by considering the IS compression and for the second interface by considering the TS_1 compression. Then the modified J model (mJ model) can be expressed as

$$\left.\begin{aligned} v_1^l &= \frac{k\Delta u_1\left\{A_t\left[Z_1 a_1^0 - (Z_2+1)a_2^0/2\right] + A_c\left[Z_1 a_1^0 + (Z_2+1)a_2^0/2\right]\right\}}{2}, \\ v_2^l &= \frac{k\Delta u_2\left\{A_t\left[Z_1 a_1^0 - (Z_2+1)a_2^0/2\right] - A_c\left[Z_1 a_1^0 + (Z_2+1)a_2^0/2\right]\right\}}{2}, \end{aligned}\right\} \tag{3.9}$$

with two new modified Atwood numbers,

$$A_t = \frac{\rho_2 - \rho_1}{\rho_2 \tanh(Z_L kL_0/2) + \rho_1} \quad \text{and} \quad A_c = \frac{\rho_2 - \rho_1}{\rho_2 \coth(Z_L kL_0/2) + \rho_1}, \tag{3.10a,b}$$

https://doi.org/10.1017/jfm.2021.438 Published online by Cambridge University Press

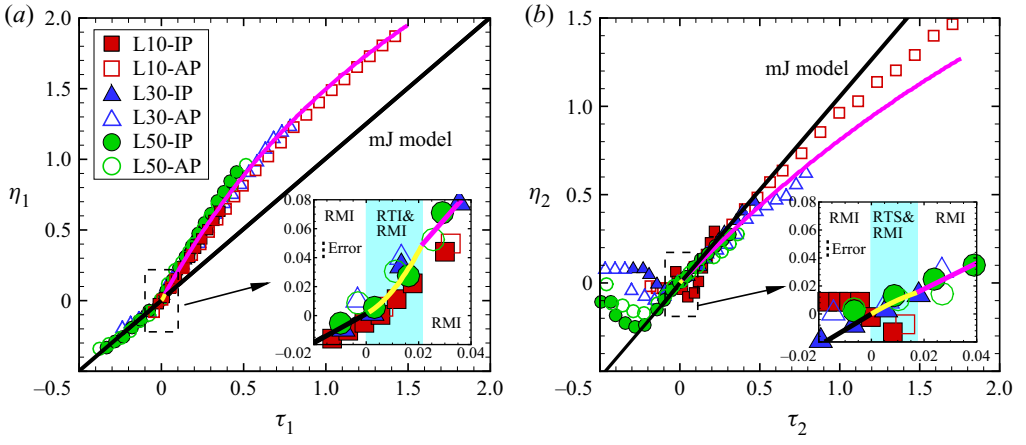


Figure 6. Comparisons of the dimensionless amplitudes of (*a*) the first interface and (*b*) the second interface. Black, yellow and purple lines represent the theoretical predictions for two interface amplitudes in the linear stage (3.9) and (3.10*a*,*b*), early nonlinear stage (3.11)–(3.15) and late nonlinear stage (3.16)–(3.18), respectively. The black dashed lines in the insets represent the scale of measurement error.

where a new compression factor $Z_L = 1 - \Delta u_1/v_{t1}$ is introduced. The values of v_1^l and v_2^l are listed in table 3, which agree well with the experimental results. As a result, the mJ model is applicable for describing the interface-coupling effect on the RMI in the linear stage.

The time-varying nonlinear amplitudes of the two interfaces are shown in figures 6(*a*) and 6(*b*), respectively. For the first interface, the time is scaled as $\tau_1 = kv_1^l(t - t_r^*)$, and the amplitude is scaled as $\eta_1 = k(a_1 - a_1^*)$ with a_1^* the amplitude of the first interface at t_r^*. For the second interface, the time is scaled as $\tau_2 = k|v_2^l|(t - t_c^*)$ and the amplitude is scaled as $\eta_2 = k(|a_2| - |a_2^*|)$ with a_2^* the amplitude of the second interface at t_c^*. The predictions of the mJ model, as shown with black lines in figures 6(*a*) and 6(*b*), underestimate the dimensionless a_1 but overestimate the dimensionless a_2 when $\tau_1 > 0$ and $\tau_2 > 0$, respectively. Therefore, the interaction of the RW with the first interface leads to the first interface being more unstable, and the interaction of the CW with the second interface results in the second interface being more stable. In addition, for the first interface, the dimensionless a_1 converges in all cases, which indicates that the fluid-layer thickness and amplitude combinations have limited influence on the nonlinear behaviour of the first interface perturbation growth. For the second interface, although the dimensionless a_2 converges in the four large L_0 cases, the dimensionless a_2 in the two $L_0 = 10$ mm cases are different and larger than the other four large L_0 cases at a late time, which indicates that the nonlinear behaviour of the second interface perturbation growth is influenced by the amplitude combination and the fluid-layer thickness when the L_0 is limited.

In the early nonlinear stage, during the interaction of the RW and the first interface, as sketched in figure 7(*a*), the light fluids outside the fluid layer accelerate the heavy fluids inside the fluid layer, which leads to the additional RTI of the first interface. In contrast, during the interaction of the CW and the second interface, the heavy fluids inside the fluid layer accelerate the light fluids outside the fluid layer, leading to the additional RTS of the second interface. The additional RTI increases the amplitude growth rate of the first interface (de Frahan *et al.* 2015; Liang *et al.* 2020*a*) but the additional RTS decreases the amplitude growth rate of the second interface. Here, we modify the ZG

https://doi.org/10.1017/jfm.2021.438 Published online by Cambridge University Press

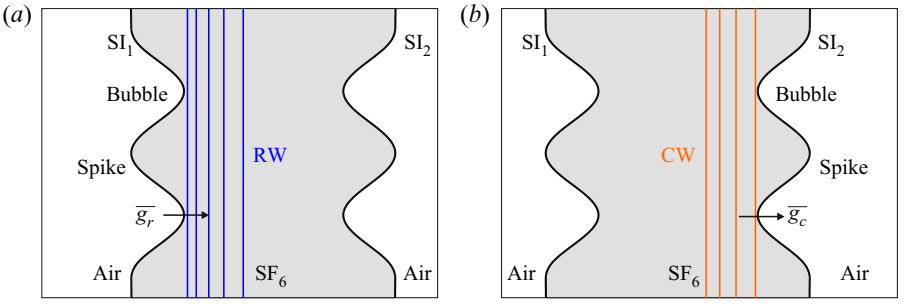


Figure 7. Sketches of (*a*) the interaction of the RW with SI_1 and (*b*) the interaction of the CW with SI_2.

model Zhang & Guo (2016) by considering the universal curves of all spikes and bubbles at any density ratio, to quantify the additional RTI of the first interface and the additional RTS of the second interface. To simplify the analysis, we consider that the RTI of the first interface and the RTS of the second interface are induced by the 1-D RW and CW, respectively. Then the expressions of the modified ZG model, i.e. the mZG model, for the first interface bubble/spike amplitude growth rate ($v^{en}_{1b/1s}$) and the second interface bubble/spike amplitude growth rate ($v^{en}_{2b/2s}$) are

$$\left.\begin{aligned}\frac{\mathrm{d}v^{en}_{1b/1s}}{\mathrm{d}t} &= -\alpha_{b/s}k\left[(v^{en}_{1b/1s})^2-(v^{qs}_{1b/1s})^2\right],\\ \frac{\mathrm{d}v^{en}_{2b/2s}}{\mathrm{d}t} &= \frac{a^0_2}{|a^0_2|}\alpha_{b/s}k\left[(v^{en}_{2b/2s})^2-(v^{qs}_{2b/2s})^2\right],\end{aligned}\right\} \tag{3.11}$$

with

$$\left.\begin{aligned}v^{qs}_{1b/1s} &= \sqrt{\frac{A\overline{g_r}}{3k}\frac{8}{(1\pm A)(3\pm A)}\frac{\left[3\pm A+\sqrt{2(1\pm A)}\right]^2}{\left[4(3\pm A)+\sqrt{2(1\pm A)}(9\pm A)\right]}},\\ v^{qs}_{2b/2s} &= \sqrt{\frac{A\overline{g_c}}{3k}\frac{8}{(1\pm A)(3\pm A)}\frac{\left[3\pm A+\sqrt{2(1\pm A)}\right]^2}{\left[4(3\pm A)+\sqrt{2(1\pm A)}(9\pm A)\right]}},\end{aligned}\right\} \tag{3.12}$$

and

$$\alpha_{b/s} = \frac{3}{4}\frac{(1\pm A)(3\pm A)}{\left[3\pm A+\sqrt{2(1\pm A)}\right]}\frac{\left[4(3\pm A)+\sqrt{2(1\pm A)}(9\pm A)\right]}{\left[\sqrt{3\pm A}+2\sqrt{2(1\pm A)}(3\mp A)\right]}. \tag{3.13}$$

The upper (lower) sign of $\pm$ and $\mp$ in all equations of this work applies to the bubble (spike). Note that the interface-coupling effect is considered because the initial $v^{en}_{1b/1s}$ equals v^l_1 at t^*_r, and the initial $v^{en}_{2b/2s}$ equals v^l_2 at t^*_c. The final bubble/spike amplitude growth rates of the two interfaces at the end of the early nonlinear stage, i.e. the bubble/spike amplitude growth rate of the first interface ($v^+_{1b/1s}$) at t^+_r, and the bubble/spike amplitude growth rate of the second interface ($v^+_{2b/2s}$) at t^+_c, are calculated with the mZG model (3.11) and (3.12), as listed in table 3. The differences between $v^+_{1b/1s}$ with v^l_1 are prominent in all cases, which indicates the effect of the RTI induced by the RW on the first interface perturbation growth is essential, regardless of a large or small fluid-layer

https://doi.org/10.1017/jfm.2021.438 Published online by Cambridge University Press

thickness. The differences between $v^{+}_{2b/2s}$ with v^{l}_{2} are prominent when the L_0 is limited, which indicates as the fluid-layer thickness decreases, the RTS induced by the CW plays an increasingly important role on influencing the second interface perturbation growth.

In addition, the RW firstly accelerates the bubble, then the spike of the first interface, as shown in figure 7(*a*). The direction of the acceleration that the RW imposes on the bubble is the same as the bubble amplitude growth. Hence, the RW decompresses the bubble before it impacts the spike of the first interface. The streamwise distance between the bubble tip with the spike tip of the first interface is $2a^{*}_{1}$, the relative velocity between the first interface and the RW head is c_1, and the first interface speed increment induced by the RW is $(u_{fn} - \Delta u_1)$. Therefore, the time-varying RW decompression effect on the first interface bubble amplitude (a_r) is

$$a_r = \frac{(u_{fn} - \Delta u_1)(t - t^{*}_{r} + a^{*}_{1}/c_1)}{2}, \tag{3.14}$$

with $(t^{*}_{r} + a^{*}_{1}/c_1) > t > (t^{*}_{r} - a^{*}_{1}/c_1)$. The CW also first accelerates the bubble, then the spike of the second interface, as shown in figure 7(*b*). However, the direction of the acceleration that the CW imposes on the bubble is the opposite of the bubble amplitude growth. Hence the CW compresses the bubble before it impacts the spike of the first interface. The streamwise distance between the bubble tip with the spike tip of the second interface is $2a^{*}_{2}$, the relative velocity between the second interface and the CW head is c^{*}_{1}, and the second interface speed increment induced by the CW is $(u_{fn} - \Delta u_2)$. Therefore, the time-varying CW compression effect on the second interface bubble amplitude (a_c) is

$$a_c = -\frac{(u_{fn} - \Delta u_2)(t - t^{*}_{c} + a^{*}_{2}/c^{*}_{1})}{2}, \tag{3.15}$$

with $(t^{*}_{c} + a^{*}_{2}/c^{*}_{1}) > t > (t^{*}_{c} - a^{*}_{2}/c^{*}_{1})$.

Based on the previous analysis, it is concluded that in the early nonlinear stage, the first interface evolution is dominated by the RMI, RTI and the decompression induced by the RW; and the second interface evolution is dominated by the RMI, RTS and the compression caused by the CW. The prediction for the a_1 by considering the additional RTI using the ZG model and the decompression induced by the RW, as shown with yellow lines in figure 6(*a*), agrees well with all experimental results. The prediction for the a_2 by considering the additional RTS using the ZG model and the compression induced by the CW, as shown with yellow lines in figure 6(*b*), agrees well with all experimental results except for the two cases with $L_0 = 10$ mm. In the L10-IP and L10-AP cases, the CW impacts the second interface before the end of the phase reversal of the second interface owing to the limited L_0. Therefore, the decrement of the dimensionless a_2 in the early nonlinear stage is mainly ascribed to the phase reversal process imposed by the RMI.

In the late nonlinear stage, after the RW tail leaves the first interface, the first interface moves with a constant speed, and therefore only the RMI dominates the first interface evolution. Similarly, after the CW tail leaves the second interface, only the RMI dominates the second interface evolution. Because the amplitudes of the two interfaces, a^{+}_{1} and a^{+}_{2}, at the end of the early nonlinear stage violate the small-amplitude prerequisite (i.e. $ka^{+}_{1} \ll 1$ and $|ka^{+}_{2}| \ll 1$), the high-amplitude effect on the nonlinear behaviour of the RMI development is non-negligible. Here, we modify the DR model (Dimonte & Ramaprabhu 2010) by considering various amplitude-wavelength ratios and density ratios to describe the late nonlinear RMI in this study. The expressions of the modified DR model, i.e. mDR

https://doi.org/10.1017/jfm.2021.438 Published online by Cambridge University Press

model, for the first interface bubble/spike amplitude growth rate ($v_{1b/1s}^{ln}$) and the second interface bubble/spike amplitude growth rate ($v_{2b/2s}^{ln}$) are

$$\left.\begin{aligned} v_{1b/1s}^{ln} &= \frac{v_{1b/1s}^{+}\left[1+(1\mp A)kv_{1b/1s}^{+}t\right]}{1+C_{1b/1s}kv_{1b/1s}^{+}t+(1\mp A)F_{b/s}(kv_{1b/1s}^{+}t)^2}, \\ v_{2b/2s}^{ln} &= \frac{v_{2b/2s}^{+}\left[1+(1\mp A)k|v_{2b/2s}^{+}|t\right]}{1+C_{2b/2s}k|v_{2b/2s}^{+}|t+(1\mp A)F_{b/s}(k|v_{2b/2s}^{+}|t)^2}, \end{aligned}\right\} \tag{3.16}$$

with

$$\left.\begin{aligned} C_{1b/1s} &= \frac{4.5\pm A+(2\mp A)ka_{1b/1s}^{+}}{4}, \\ C_{2b/2s} &= \frac{4.5\pm A+(2\mp A)k|a_{2b/2s}^{+}|}{4}, \end{aligned}\right\} \tag{3.17}$$

and

$$F_{b/s}=1\pm A. \tag{3.18}$$

The mDR model predictions for a_1 and a_2 are shown in figures 6(a) and 6(b) with purple lines, respectively, and agree well with all experimental results for the first interface, and the four large L_0 cases for the second interface. As the RTI and decompression effect induced by the RW promote the first interface perturbation growth, and the RTS and compression effect caused by the CW suppress the second interface perturbation growth, the a_1 is larger than the a_2 in all cases. In addition, bubbles of the two interfaces coalesce in the L10-IP case, and all structures of two interfaces combine in the L10-AP case at a late time, as shown in figures 5(e) and 5(f). As a result, the second interface perturbation growths are promoted by the first interface counterpart in the L10-IP and L10-AP cases, and which exceed the mDR model predictions. Overall, the a_2 in the L10-IP and L10-AP cases is smaller than the a_1 but larger than the mDR model prediction.

4. Conclusions

Experimental and theoretical studies on an air/SF_6/air fluid layer with a finite thickness have been performed to investigate the wave patterns, interface motions and interfacial instabilities of both sides of a fluid layer. Experimentally, the extended soap-film technique has been utilised in a shock tube to create three kinds of quasi-1-D layers with different layer thicknesses, and six kinds of quasi-2-D layers with diverse layer thicknesses and amplitude combinations. We have adopted schlieren photography and have used a high-speed camera to capture experimental pictures. The RW and CW going back and forth inside fluid layers have been identified.

First, wave patterns and interface motions in the three quasi-1-D heavy-fluid-layer cases have been studied. The RW reflected from the second interface accelerates the first interface, and the CW reflected from the first interface accelerates the second interface. Finally, all waves refract outside the fluid layer and the two interfaces of the fluid layer move with a same speed. A general 1-D theory is established to describe the two interfaces'

https://doi.org/10.1017/jfm.2021.438 Published online by Cambridge University Press

motions in three stages: (I) uniform motion with the post-shock velocity, (II) acceleration induced by the RW or CW and (III) uniform motion with the final speed.

Second, the morphologies of the two interfaces of a quasi-2-D heavy fluid layer induced by a shock wave are investigated. The final phase of the second interface is opposite of that of the first interface when the initial amplitudes of the two interfaces are the same, whereas the final phase of the second interface is the same as that of the first interface when the initial amplitudes of the two interfaces are the opposite. For the first time, it is observed experimentally that local or whole structures of the two interfaces coalesce when the initial fluid layer is very thin.

Third, the interfacial instabilities of a quasi-2-D heavy fluid layer are examined, which can be divided into three stages. (I) Linear stage. Before the RW impacts the first interface, or before the CW impacts the second interface, only the RMI dominates the perturbation growth of the first interface, or the second interface. (II) Early nonlinear stage. During the interaction of the RW and the first interface, the RMI, the RTI and the decompression effect induced by the RW dominate the first interface perturbation growth. During the interaction of the CW and the second interface, the RMI, the RTS and the compression effect induced by the CW dominate the second interface perturbation growth. The RW destabilises the first interface, but the CW stabilises the second interface. (III) Late nonlinear stage. After the RW passes the first interface, or after the CW passes the second interface, only the RMI dominates the perturbation growth of the first interface, or the second interface.

Fourth, linear and nonlinear models are successfully established by considering the interface-coupling effect on the RMI, and the additional interfacial instabilities induced by these waves inside the heavy fluid layer. The linear amplitude growths of the two interfaces can be well described by the mJ model considering the interface-coupling effect and the post-shock parameters. The early nonlinear perturbation growth on the first interface can be characterised by the sum of the mZG model prediction for quantifying the additional RTI and the decompression effect on the first interface bubble amplitude. The early nonlinear perturbation growth on the second interface can be described by a sum of the mZG model prediction for quantifying the additional RTS and the compression effect on the second interface bubble amplitude. The late nonlinear perturbation growths on the two interfaces can be characterised by the mDR model. As local or whole structures of the first interface and second interface coalesce and the amplitude growth rate of the first interface is larger than that of the second interface, the nonlinear perturbation growth of the second interface of a thin fluid layer is promoted by the first interface counterpart and exceeds the mDR model prediction. It is worth looking forward to testing the proposed models in this study with more experiments by varying the shock strengths, amplitudes, wavenumbers and phases of the perturbations on the two interfaces.

Funding. This work was supported by Tamkeen under the NYU Abu Dhabi Research Institute grant CG002 and the Natural Science Foundation of China (grant numbers 11772329, 91952205 and 11625211). The authors are grateful to Dr L. Liu's help on performing experiments.

Declaration of interests. The authors report no conflict of interest.

Author ORCIDs.
Yu Liang https://orcid.org/0000-0002-3254-7073;
Xisheng Luo https://orcid.org/0000-0002-4303-8290.

https://doi.org/10.1017/jfm.2021.438 Published online by Cambridge University Press

References

Banerjee, A. 2020 Rayleigh–Taylor instability: a status review of experimental designs and measurement diagnostics. *Trans. ASME J. Fluids Engng* **142** (12), 120801.

Bell, G.I. 1951 Taylor instability on cylinders and spheres in the small amplitude approximation. *Rep. No. LA-1321*, LANL 1321.

Brouillette, M. 2002 The Richtmyer–Meshkov instability. *Annu. Rev. Fluid Mech.* **34**, 445–468.

Budzinski, J.M., Benjamin, R.F. & Jacobs, J.W. 1994 Influence of initial conditions on the flow patters of a shock-accelerated thin fluid layer. *Phys. Fluids* **6**, 3510–3512.

Dimonte, G. & Ramaprabhu, P. 2010 Simulations and model of the nonlinear Richtmyer–Meshkov instability. *Phys. Fluids* **22**, 014104.

Ding, J., Li, J., Sun, R., Zhai, Z. & Luo, X. 2019 Convergent Richtmyer–Meshkov instability of a heavy gas layer with perturbed outer interface. *J. Fluid Mech.* **878**, 277–291.

Drake, R.P. 2018 *High-Energy-Density Physics: Foundation of Inertial Fusion and Experimental Astrophysics*. Springer.

de Frahan, M.T.H., Movahed, P. & Johnsen, E. 2015 Numerical simulations of a shock interacting with successive interfaces using the discontinuous galerkin method: the multilayered Richtmyer–Meshkov and Rayleigh–Taylor instabilities. *Shock Waves* **25** (4), 329–345.

Han, Z. & Yin, X. 1993 *Shock Dynamics*. Kluwer Academic Publishers and Science Press.

Jacobs, J.W., Jenkins, D.G., Klein, D.L. & Benjamin, R.F. 1995 Nonlinear growth of the shock-accelerated instability of a thin fluid layer. *J. Fluid Mech.* **295**, 23–42.

Jacobs, J.W., Klein, D.L., Jenkins, D.G. & Benjamin, R.F. 1993 Instability growth patterns of a shock-accelerated thin fluid layer. *Phys. Rev. Lett.* **70**, 583–586.

Kuranz, C.C., *et al.*, 2018 How high energy fluxes may affect Rayleigh–Taylor instability growth in young supernova remnants. *Nat. Commun.* **9**, 1564.

Li, J., Ding, J., Si, T. & Luo, X. 2020 Convergent Richtmyer–Meshkov instability of light gas layer with perturbed outer surface. *J. Fluid Mech.* **884**, R2.

Liang, Y., Liu, L., Zhai, Z., Si, T. & Wen, C.-Y. 2020*a* Evolution of shock-accelerated heavy gas layer. *J. Fluid Mech.* **886**, A7.

Liang, Y., Zhai, Z., Ding, J. & Luo, X. 2019 Richtmyer–Meshkov instability on a quasi-single-mode interface. *J. Fluid Mech.* **872**, 729–751.

Liang, Y., Zhai, Z., Luo, X. & Wen, C. 2020*b* Interfacial instability at a heavy/light interface induced by rarefaction waves. *J. Fluid Mech.* **885**, A42.

Lindl, J., Landen, O., Edwards, J., Moses, E. & Team, N. 2014 Review of the national ignition campaign 2009–2012. *Phys. Plasmas* **21**, 020501.

Liu, L., Liang, Y., Ding, J., Liu, N. & Luo, X. 2018*a* An elaborate experiment on the single-mode Richtmyer–Meshkov instability. *J. Fluid Mech.* **853**, R2.

Liu, W., Li, X., Yu, C., Fu, Y., Wang, P., Wang, L. & Ye, W. 2018*b* Theoretical study on finite-thickness effect on harmonics in Richtmyer–Meshkov instability for arbitrary Atwood numbers. *Phys. Plasmas* **25** (12), 122103.

Luo, X., Liang, Y., Si, T. & Zhai, Z. 2019 Effects of non-periodic portions of interface on Richtmyer–Meshkov instability. *J. Fluid Mech.* **861**, 309–327.

Luo, X., Zhang, F., Ding, J., Si, T., Yang, J., Zhai, Z. & Wen, C. 2018 Long-term effect of Rayleigh–Taylor stabilization on converging Richtmyer–Meshkov instability. *J. Fluid Mech.* **849**, 231–244.

Meshkov, E.E. 1969 Instability of the interface of two gases accelerated by a shock wave. *Fluid Dyn.* **4**, 101–104.

Meyer, K.A. & Blewett, P.J. 1972 Numerical investigation of the stability of a shock-accelerated interface between two fluids. *Phys. Fluids* **15**, 753–759.

Mikaelian, K.O. 1982 Normal modes and symmetries of the Rayleigh–Taylor instability in stratified fluids. *Phys. Rev. Lett.* **48** (19), 1365.

Mikaelian, K.O. 1985 Richtmyer–Meshkov instabilities in stratified fluids. *Phys. Rev.* A **31**, 410–419.

Mikaelian, K.O. 1990 Rayleigh–Taylor and Richtmyer–Meshkov instabilities in multilayer fluids with surface tension. *Phys. Rev.* A **42** (12), 7211.

Mikaelian, K.O. 1995 Rayleigh–Taylor and Richtmyer–Meshkov instabilities in finite-thickness fluid layers. *Phys. Fluids* **7** (4), 888–890.

Mikaelian, K.O. 1996 Numerical simulations of Richtmyer–Meshkov instabilities in finite-thickness fluid layers. *Phys. Fluids* **8** (5), 1269–1292.

Morgan, R.V., Cabot, W.H., Greenough, J.A. & Jacobs, J.W. 2018 Rarefaction-driven Rayleigh–Taylor instability. Part 2. Experiments and simulations in the nonlinear regime. *J. Fluid Mech.* **838**, 320–355.

https://doi.org/10.1017/jfm.2021.438 Published online by Cambridge University Press

MORGAN, R.V., LIKHACHEV, O.A. & JACOBS, J.W. 2016 Rarefaction-driven Rayleigh–Taylor instability. Part 1. Diffuse-interface linear stability measurements and theory. *J. Fluid Mech.* **791**, 34–60.

OLMSTEAD, D., WAYNE, P., YOO, J.-H., KUMAR, S., TRUMAN, C.R. & VOROBIEFF, P. 2017 Experimental study of shock-accelerated inclined heavy gas cylinder. *Exp. Fluids* **58** (6), 71.

OTT, E. 1972 Nonlinear evolution of the Rayleigh–Taylor instability of a thin layer. *Phys. Rev. Lett.* **29** (21), 1429.

PLESSET, M.S. 1954 On the stability of fluid flows with spherical symmetry. *J. Appl. Phys.* **25**, 96–98.

PRESTRIDGE, K., VOROBIEFF, P., RIGHTLEY, P.M. & BENJAMIN, R.F. 2000 Validation of an instability growth model using particle image velocimtery measurement. *Phys. Rev. Lett.* **84**, 4353–4356.

RAYLEIGH, L. 1883 Investigation of the character of the equilibrium of an incompressible heavy fluid of variable density. *Proc. Lond. Math. Soc.* **14**, 170–177.

RICHTMYER, R.D. 1960 Taylor instability in shock acceleration of compressible fluids. *Commun. Pure Appl. Maths* **13**, 297–319.

ROMERO, B.E., POROSEVA, S., VOROBIEFF, P. & REISNER, J. 2021 Shock driven Kelvin–Helmholtz instability. In *AIAA Scitech 2021 Forum*, p. 0051. AIAA.

SHARP, D.H. 1984 An overview of Rayleigh–Taylor instability. *Physica* D **12** (1), 3–18.

SUN, R., DING, J., ZHAI, Z., SI, T. & LUO, X. 2020 Convergent Richtmyer–Meshkov instability of heavy gas layer with perturbed inner surface. *J. Fluid Mech.* **902**, A3.

TAYLOR, G. 1950 The instability of liquid surfaces when accelerated in a direction perpendicular to their planes. I. *Proc. R. Soc. Lond.* A **201** (1065), 192–196.

VELIKOVICH, A. & PHILLIPS, L. 1996 Instability of a plane centered rarefaction wave. *Phys. Fluids* **8** (4), 1107–1118.

WANG, L., GUO, H., WU, J., YE, W., LIU, J., ZHANG, W. & HE, X. 2014 Weakly nonlinear Rayleigh–Taylor instability of a finite-thickness fluid layer. *Phys. Plasmas* **21** (12), 122710.

ZHAI, Z., ZOU, L., WU, Q. & LUO, X. 2018 Review of experimental Richtmyer–Meshkov instability in shock tube: from simple to complex. *Proc. Inst. Mech. Engrs* **232**, 2830–2849.

ZHANG, Q. & GUO, W. 2016 Universality of finger growth in two-dimensional Rayleigh–Taylor and Richtmyer–Meshkov instabilities with all density ratios. *J. Fluid Mech.* **786**, 47–61.

ZHOU, Y. 2017*a* Rayleigh–Taylor and Richtmyer–Meshkov instability induced flow, turbulence, and mixing. I. *Phys. Rep.* **720–722**, 1–136.

ZHOU, Y. 2017*b* Rayleigh–Taylor and Richtmyer–Meshkov instability induced flow, turbulence, and mixing. II. *Phys. Rep.* **723–725**, 1–160.

https://doi.org/10.1017/jfm.2021.438 Published online by Cambridge University Press